



Numerical Simulations on the Deflection of Coronal Mass Ejections in the Interplanetary Space

Bin Zhuang^{1,2} , Yuming Wang^{1,2} , Youqiu Hu¹, Chenglong Shen^{1,2,3}, Rui Liu^{1,2,3,4} , Tingyu Gou^{1,2} ,
Quanhao Zhang^{1,2} , and Xiaolei Li^{1,2}

¹ CAS Key Laboratory of Geospace Environment, Department of Geophysics and Planetary Sciences, University of Science and Technology of China, Hefei 230026, People's Republic of China; zbzb@mail.ustc.edu.cn, yumwang@ustc.edu.cn

² CAS Center for Excellence in Comparative Planetology, Hefei 230026, People's Republic of China

³ Mengcheng National Geophysical Observatory, School of Earth and Space Sciences, University of Science and Technology of China, Hefei 230026, People's Republic of China

⁴ Collaborative Innovation Center of Astronautical Science and Technology, Hefei 230026, People's Republic of China

Received 2019 January 2; revised 2019 March 25; accepted 2019 March 25; published 2019 May 6

Abstract

Deflection of coronal mass ejections (CMEs) in the interplanetary space, especially in the ecliptic plane, serves as an important factor deciding whether CMEs arrive at the Earth. Observational studies have shown evidence for deflection, whose detailed dynamic processes, however, remain obscure. Here we developed a 2.5D ideal magnetohydrodynamic simulation to study the propagation of CMEs traveling with different speeds in the heliospheric equatorial plane. The simulation confirms the existence of the CME deflection in the interplanetary space, which is related to the difference between the CME speed (v_r) and the solar wind speed (v_{sw}): a CME will propagate radially as v_r is close to v_{sw} but eastward or westward when v_r is larger or smaller than v_{sw} ; the greater the difference is, the larger the deflection angle will be. This result supports the model for CME deflection in the interplanetary space (DIPS) proposed by Wang et al., predicting that an isolated CME can be deflected due to the pileup of solar wind plasma ahead of or behind the CME. Furthermore, the deflection angles, which are derived by inputting v_r and v_{sw} from the simulation into the DIPS model, are found to be consistent with those in the simulation.

Key words: methods: numerical – Sun: coronal mass ejections (CMEs)

1. Introduction

The arrival of coronal mass ejections (CMEs) at the Earth plays an important role for the geospace environment, since CMEs carry a huge amount of mass, magnetic flux, and energy, and are capable of producing geomagnetic storms (Gosling et al. 1990; Srivastava & Venkatakrishnan 2004) and other hazardous space weather phenomena. It was once thought that CMEs, originating from solar source regions facing the Earth, would propagate along the Sun–Earth line (Howard et al. 1982) and then hit the Earth. However, only 65%–80% of these types of CMEs were found to finally arrive at the Earth (Wang et al. 2002; Yermolaev & Yermolaev 2006, and references therein). On the contrary, the Earth-encountered limb CMEs also exist (Webb et al. 2000; Zhang et al. 2003; Cid et al. 2012; Wang et al. 2014, 2016). The CME deflection in the corona and interplanetary space serves as a promising reason for those arrival variations.

One cause of the CME deflections is the CME–CME interaction (Lugaz et al. 2012, 2017; Shen et al. 2012, 2017), associated with a deflection angle of 10° or even larger. A single CME is also believed to be possibly deflected by background solar wind and magnetic field. In the corona where the magnetic field is dominant, the CME deflection caused by the asymmetric distribution of the background magnetic field has been widely studied (e.g., Cremades & Bothmer 2004; Lugaz et al. 2011; Wang et al. 2011; Zuccarello et al. 2012; DeForest et al. 2013; Kay et al. 2013; Zhou & Feng 2013; Möstl et al. 2015; Capannolo et al. 2017). For example, Gui et al. (2011) and Shen et al. (2011) found that a CME could be deflected due to the gradient of the corona magnetic energy density by more than 20° . However, whether or not an isolated CME can be deflected in the interplanetary space, where the solar wind becomes dominant and the magnetic fields decrease with distance, is still under

debate. Several studies have reported the cases of CMEs experiencing such deflection by combining coronagraph and in situ observations (Wang et al. 2006, 2014; Lugaz 2010; Wang et al. 2016). To describe how a CME is deflected in the interplanetary space and ecliptic plane, Wang et al. (2004, 2014) proposed a model for CME deflection in the interplanetary space (DIPS), predicting that a CME traveling faster or slower than the ambient solar wind will be deflected toward the east or west due to the pileup of solar wind plasma ahead of or behind the CME. Based on this model, two CME events with anomalous geoeffectiveness were studied. First is a slow CME on 2008 September 13, originating from the east limb of the solar disk. It was found to be deflected by more than 20° toward the west in the interplanetary space, enhancing the probability of the CME encountering the Earth (Wang et al. 2014). Second is the unexpected and largest geomagnetic storm in solar cycle 24, referred to as the 2015 St. Patrick's Day event, caused by a CME that was initially west-oriented and then deflected toward the Earth, increasing its geoeffectiveness (Wang et al. 2016). Furthermore, Zhuang et al. (2017) developed an automated CME arrival forecasting system with the DIPS model incorporated, and found that the success rate of the CME arrival predictions is about 82% with deflection considered, which is 19% higher than that without deflection. These results indicate the importance of CME deflections in space weather research.

The understanding of the CME propagation has been largely improved by the development of magnetohydrodynamic (MHD) simulation techniques (e.g., Vandas et al. 1996; Riley et al. 2003; Manchester et al. 2004a; Wu et al. 2007; Xiong et al. 2007; Shiota et al. 2010; Lugaz et al. 2011; Zuccarello et al. 2012; Shen et al. 2013, 2014; Zhou & Feng 2013; Shiota & Kataoka 2016; Zhou & Feng 2017). Among these studies, some

focused on the CME deflection near the Sun or in the heliospheric meridional plane. For example, Zhou & Feng (2017) used a three-dimensional (3D) MHD simulation to show that CMEs tend to be deflected toward the heliospheric current sheet (HCS) in the latitudinal direction near the Sun and then propagate almost parallel to the HCS in the interplanetary space. As for the CME deflection in the ecliptic plane, Vandas et al. (1996) found that a CME could be deflected to the side where it meets the external interplanetary magnetic field polarity that is opposite to the field of itself. This deflection is probably due to the reconnection between the magnetic field lines of the CME and background. Shiota & Kataoka (2016) simulated the interplanetary propagation of multiple CMEs and found that one was strongly deflected by the inhomogeneity of the background solar wind, and this inhomogeneity was caused by the preceding eruption. Recently, Török et al. (2018) developed a Sun-to-Earth MHD simulation to study the 2000 July 14 ‘‘Bastille Day’’ eruption and found that the corresponding CME experienced no significant deflection of the trajectory in the longitudinal direction. They suggested that this phenomenon may be because (1) a fast CME should be less susceptible to deflection than a slow one, or (2) there existed a suppression of a significant pileup of flux by continuous reconnection between the CME and the interplanetary magnetic field. Although these studies have exposed the (non)deflection of CMEs to some extent, there is still a lack of knowledge about how a single CME is deflected only by the background solar wind. Besides, could the potential deflection of a slow or fast CME be similar to that suggested by the DIPS model? Our work will focus on these questions.

In this work, we study the CME propagation by developing a 2.5D ideal MHD simulation of the flux rope/solar wind system in the heliospheric equatorial plane. The simulation is based on the following two considerations. First, CMEs are believed to have a flux rope topology (Chen et al. 1997; Dere et al. 1999; Forbes 2000; Chen & Krall 2003; Vourlidis et al. 2013), and the model of flux rope driven CME was successfully used in some simulation studies (e.g., Manchester et al. 2004a, 2004b; Chané et al. 2006; Shiota et al. 2010). Second, a 2.5D MHD simulation instead of a 3D one is simple and effective when we only consider the deflection of CMEs in the equatorial plane. The organization of this paper is as follows. We give a brief description about the MHD equations in Section 2. The simulation method and the corresponding results are introduced in Section 3. In Section 4, we compare our simulated results with the predictions estimated by the DIPS model. We provide our conclusions and discussions in Section 5.

2. MHD Equations in the Heliospheric Equatorial Plane

We take spherical coordinate (r, θ, ϕ) and consider 2.5D ($\frac{\partial}{\partial \theta} = 0$) problems in the heliospheric equatorial plane ($\theta = \pi/2$). The 2.5D ideal MHD equations are given as follows:

$$\frac{\partial \rho}{\partial t} + \mathbf{v} \cdot \nabla \rho + \rho \nabla \cdot \mathbf{v} = 0, \quad (1)$$

$$\frac{\partial \mathbf{v}}{\partial t} + \mathbf{v} \cdot \nabla \mathbf{v} + R \nabla T + \frac{RT}{\rho} \nabla \rho - \frac{1}{\mu_0 \rho} (\nabla \times \mathbf{B}) \times \mathbf{B} - \frac{GM_s}{r^2} \hat{\mathbf{r}} = 0, \quad (2)$$

$$\frac{\partial \mathbf{B}}{\partial t} - \nabla \times (\mathbf{v} \times \mathbf{B}) = 0, \quad (3)$$

$$\frac{\partial T}{\partial t} + \mathbf{v} \cdot \nabla T + (\gamma - 1) T \nabla \cdot \mathbf{v} = 0, \quad (4)$$

where ρ , \mathbf{v} , T , and \mathbf{B} represent density, flow velocity, temperature, and magnetic field, respectively. R is the gas constant, μ_0 is the magnetic permeability of free space, G is the gravitational constant, M_s is the mass of the Sun, and γ is the polytropic index that is set to be 1.05, aimed at adding an extraneous heating of the solar corona and necessary for supersonic solar wind solutions.

We perform our simulation in the frame that corotates with the Sun. The flow velocity in this frame (\mathbf{u}) can be written as

$$\mathbf{u} = (u_r, u_\theta, u_\phi), \quad u_r = v_r, \quad u_\theta = v_\theta, \\ u_\phi = v_\phi - \Omega r, \quad (5)$$

where $\Omega = 2.865 \times 10^{-6}$ radian s^{-1} serves as the self-rotation speed of the Sun. Note that v_ϕ of the solar wind is very small of a few km s^{-1} , compared to v_r and v_θ . To derive a better precision of the flow speed in the ϕ direction, \mathbf{u} is replaced by \mathbf{v} in the simulation. The corresponding MHD equations are then modified by adding the terms of $(-\Omega \partial U / \partial \phi)$ on the left sides of Equations (1)–(4), where $U = (\rho, v_r, v_\theta, v_\phi, \psi, B_\theta, T)$ and ψ is the magnetic flux function. \mathbf{B} can be expressed by

$$\mathbf{B} = \nabla \psi \times \frac{\mathbf{e}_\theta}{r} + \mathbf{B}_\theta, \quad \text{and } \mathbf{B}_\theta = B_\theta \hat{\theta}. \quad (6)$$

Finally, we arrive at the equations in the r and ϕ directions as:

$$\frac{\partial \rho}{\partial t} + v_r \frac{\partial \rho}{\partial r} + \frac{v_\phi}{r} \frac{\partial \rho}{\partial \phi} + \rho \frac{\partial v_r}{\partial r} + \frac{\rho}{r} \frac{\partial v_\phi}{\partial \phi} \\ + \frac{2\rho v_r}{r} - \Omega \frac{\partial \rho}{\partial \phi} = 0, \quad (7)$$

$$\frac{\partial v_r}{\partial t} + v_r \frac{\partial v_r}{\partial r} + \frac{v_\phi}{r} \frac{\partial v_r}{\partial \phi} + \frac{RT}{\rho} \frac{\partial \rho}{\partial r} + R \frac{\partial T}{\partial r} + \frac{\mathcal{L}\psi}{\mu_0 \rho} \frac{\partial \psi}{\partial r} \\ + \frac{B_\theta}{\mu_0 \rho} \frac{\partial B_\theta}{\partial r} + \frac{B_\theta^2}{\mu_0 \rho r} - \frac{v_\theta^2 + v_\phi^2}{r} + \frac{GM_s}{r^2} - \Omega \frac{\partial v_r}{\partial \phi} = 0, \quad (8)$$

$$\frac{\partial v_\phi}{\partial t} + v_r \frac{\partial v_\phi}{\partial r} + \frac{v_\phi}{r} \frac{\partial v_\phi}{\partial \phi} + \frac{RT}{\rho r} \frac{\partial \rho}{\partial \phi} + \frac{R}{r} \frac{\partial T}{\partial \phi} \\ + \frac{\mathcal{L}\psi}{\mu_0 \rho r} \frac{\partial \psi}{\partial \phi} + \frac{B_\theta}{\mu_0 \rho r} \frac{\partial B_\theta}{\partial \phi} + \frac{v_r v_\theta}{r} - \Omega \frac{\partial v_\phi}{\partial \phi} = 0, \quad (9)$$

$$\frac{\partial v_\theta}{\partial t} + v_r \frac{\partial v_\theta}{\partial r} + \frac{v_\theta}{r} \frac{\partial v_\theta}{\partial \phi} \\ + \frac{1}{\mu_0 \rho r^2} \left(\frac{\partial \psi}{\partial \phi} \frac{\partial B_\theta}{\partial r} - \frac{\partial \psi}{\partial r} \frac{\partial B_\theta}{\partial \phi} \right) \\ + \frac{B_\theta}{\mu_0 \rho r^3} \frac{\partial \psi}{\partial \phi} + \frac{v_r v_\theta}{r} - \Omega \frac{\partial v_\theta}{\partial \phi} = 0, \quad (10)$$

$$\frac{\partial \psi}{\partial t} + v_r \frac{\partial \psi}{\partial r} + \frac{v_\phi}{r} \frac{\partial \psi}{\partial \phi} - \Omega \frac{\partial \psi}{\partial \phi} = 0, \quad (11)$$

$$\begin{aligned} \frac{\partial B_\theta}{\partial t} + v_r \frac{\partial B_\theta}{\partial r} + \frac{v_\phi}{r} \frac{\partial B_\theta}{\partial \phi} + B_\theta \left(\frac{\partial v_r}{\partial r} + \frac{1}{r} \frac{\partial v_\phi}{\partial \phi} \right) \\ + \frac{v_r B_\theta}{r} + \frac{1}{r^2} \left(\frac{\partial \psi}{\partial \phi} \frac{\partial v_\theta}{\partial r} - \frac{\partial \psi}{\partial r} \frac{\partial v_\theta}{\partial \phi} \right) \\ - \frac{v_\theta}{r^3} \frac{\partial \psi}{\partial \phi} - \Omega \frac{\partial B_\theta}{\partial \phi} = 0, \end{aligned} \quad (12)$$

$$\begin{aligned} \frac{\partial T}{\partial t} + v_r \frac{\partial T}{\partial r} + \frac{v_\phi}{r} \frac{\partial T}{\partial \phi} + (\gamma - 1) T \left(\frac{\partial v_r}{\partial r} + \frac{1}{r} \frac{\partial v_\phi}{\partial \phi} \right) \\ + \frac{2(\gamma - 1) T v_r}{r} - \Omega \frac{\partial T}{\partial \phi} = 0, \end{aligned} \quad (13)$$

$$\text{and } \mathcal{L} \equiv \frac{1}{r^2} \left(\frac{\partial^2}{\partial r^2} + \frac{1}{r^2} \frac{\partial^2}{\partial \phi^2} \right). \quad (14)$$

We take the density of $\rho_0 = 2.505 \times 10^{-13} \text{ kg m}^{-3}$, the temperature of $T_0 = 1 \times 10^6 \text{ K}$, and the solar radius of $R_s = 6.965 \times 10^8 \text{ m}$ as the basic units. Other numerical units are derived as follows:

$$\begin{aligned} v_0 &= \sqrt{RT_0} = 1.286 \times 10^5 \text{ m s}^{-1}, \\ t_0 &= R_s / v_0 = 5.416 \times 10^3 \text{ s}, \\ M_0 &= \rho_0 R_s^3 = 8.464 \times 10^{13} \text{ kg}, \\ B_0 &= \sqrt{\mu_0 \rho_0 v_0^2} = 7.216 \times 10^{-5} \text{ T}, \text{ and} \\ \psi_0 &= B_0 R_s^2 = 3.500 \times 10^{13} \text{ Wb}. \end{aligned}$$

3. Simulation Method and Results of the Flux Rope System

The above MHD equations are solved by the multistep implicit scheme (Hu 1989). Here we give a brief description about this scheme in the Appendix. We set the computational domain as $1 \leq r \leq 305$, $0 \leq \phi \leq \pi$, discretized into 215×92 grid points. The grid spacing along the radial direction is set to be uniform, 0.625 in between $r = 10$ and 30, 3 in between $r = 140$ and 305, and increases according to a geometric series of a common ratio 1.0689 in between $r = 1$ and 10 and 1.0207 in between $r = 30$ and 140. A uniform mesh is adopted in the ϕ direction. ρ , v_r , v_θ , v_ϕ , B_θ , and T at $\phi = 0^\circ$ share the same values as those at $\phi = 180^\circ$, but the values of ψ on the left and right sides of the domain are opposite. The simulation is processed by the following sequences: (1) a solar wind background with a fully open magnetic field is constructed; (2) a flux rope is introduced; (3) the eruption of flux rope is triggered by the catastrophe of the system; (4) the speed of the rope is adjusted during its propagation. In this work, the CME structure is characterized only by the flux rope, though DeForest et al. (2013) used the term ‘‘CME’’ including not only the flux rope, but also the surrounding sheath material and any other solar wind or coronal material entrained en route.

3.1. Construction of the Solar Wind Background

Previous works have studied the flux rope system in the solar wind background with partly open magnetic field in the heliospheric meridional plane (Hu et al. 2003; Sun & Hu 2005; Chen et al. 2007). Shifting to the equatorial plane, a fully open magnetic field for studying the propagation of the flux rope can be obtained by modifying the related ψ to open up all the closed magnetic field lines. At the base, the density and

temperature are set to be 1 and 1.5, respectively. The distribution of $\psi(t, 1, \phi)$ is equal to $\psi_r \sin(\phi)/2$, where $\psi_r \equiv \pi (215 R_s)^2 B_{rE} = 2.325 \times 10^{14} \text{ Wb} = 6.643 \psi_0$, and $B_{rE} = 3.3 \times 10^{-9} \text{ T}$ indicating the initial magnetic field strength at the distance of 1 au. At the top, we apply the linear extrapolation to all the quantities. Figure 1 shows the magnetic structure of the steady solar wind solution in the frame corotating with the Sun. The solid white lines depict the magnetic field lines and the arrows indicate the related field directions. Spiral magnetic field structure in the interplanetary space can be seen. The field lines going upward from and downward to the solar surface form the fully open field. The density and flow velocity magnitude of the solar wind plasma, shown in false color, are found to be larger and smaller in the region embedded with the magnetic field with opposite directions (clearly seen at lower distance), respectively.

3.2. Eruption of the Flux Rope Driven CME

After constructing the solar wind background, a flux rope is then introduced into the system with given (Φ_p, Φ_z, M) of the rope, where Φ_p is the poloidal magnetic flux per unit radian, Φ_z is axial magnetic flux, and M is the mass per unit radian. We set $(\Phi_p, \Phi_z, M) = (0.5, 0.3, 0.5)$. One can refer to Hu et al. (2003) to find the method of introducing a flux rope. The rope is attached to the solar surface and centered at $\phi = 90^\circ$ initially, as shown in Figure 2. The region of the flux rope is determined by $\psi \geq \psi_r / 2 = 3.322 \psi_0$. The magnetic field on the left and right sides of the rope shares the same upward and downward directions with the background magnetic field. The mass inside the flux rope is distributed in the rope lower part due to the gravity, and the rope forms an oval-shape, which is different from the circular shape with overlying arcade on the rope top as shown in Hu et al. (2003).

In this work, the eruption of the flux rope is triggered by the catastrophe. The catastrophe of the flux rope system has been widely studied (e.g., Hu 2001; Hu et al. 2003; Sun & Hu 2005; Zhang et al. 2017; Zhuang et al. 2018), giving that the increase in Φ_p and Φ_z or the decrease in M of the rope can lead to the catastrophe and the sudden release of the rope. We increase Φ_p to 0.9 for triggering the catastrophe. During the rope propagation, Φ_p , Φ_z and M are maintained as constants and magnetic reconnection is prohibited. These adjustments make sense for our study because we focus on the characteristics of the rope propagation. In reality, the rope may experience an erosion process (e.g., Dasso et al. 2006; Ruffenach et al. 2012, 2015; Wang et al. 2018) through the magnetic reconnection with the ambient solar wind (Gosling 2012), causing the erosion of the magnetic flux. Figure 3 shows the propagation of the flux rope in the interplanetary space in the laboratory frame. We use $t = 0$ to indicate the condition when the flux rope just starts to erupt. We can see that the eruption results in (1) an envelope composed of interplanetary magnetic field draping around the rope and (2) a large sheath ahead of the rope indicated by the region with larger velocity magnitude. This rope propagates at a speed close to the ambient solar wind speed. We find that the rope experiences no significant deflection during its propagation. However, the front part and the tail part of the rope are found to be stretched to the east and west, respectively, which may be caused by the interaction with the background.

Figure 4(a) plots the variations of the longitudes of the front, the axis (defined by the maximum ψ inside the rope), and the mass center of the flux rope along the front radial distance.

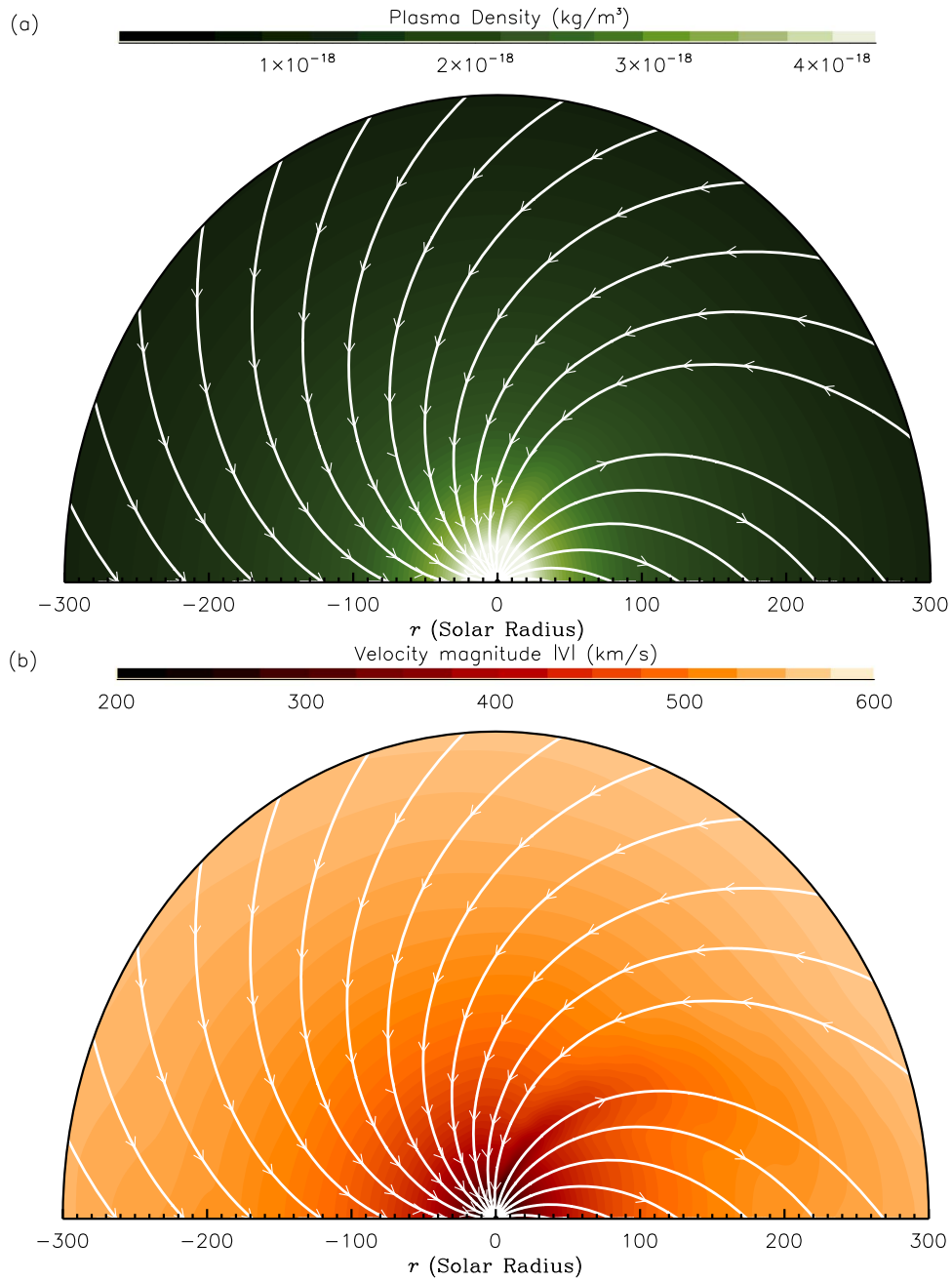


Figure 1. Magnetic structure of the steady solar wind solution in a frame corotating with the Sun. Solid white lines depict the magnetic field lines and the arrows indicate the related field directions, and the plasma density and velocity magnitude of the solar wind medium are shown in false color. The density and speed are saturated at values indicated by the color bars.

Note that here the front is defined by the uppermost closed field line of the rope along the Sun-axis line so as to avoid the stretched rope region, making the symbols of the front and axis overlapped with each other. The mass center (r_c, ϕ_c) is calculated by

$$\begin{aligned}
 x_i &= r_i \cos \phi_i, \quad y_i = r_i \sin \phi_i, \quad m_i = \rho r_i dr_i d\phi, \\
 x_c &= \frac{\sum m_i x_i}{\sum m_i}, \quad y_c = \frac{\sum m_i y_i}{\sum m_i}, \\
 r_c &= \sqrt{x_c^2 + y_c^2} \quad \text{and} \quad \phi_c = \pi/2 - \arctan(x_c/y_c). \quad (15)
 \end{aligned}$$

Here (r_i, ϕ_i) shows the position of a grid inside the rope in the laboratory frame, $dr_i = (r_{i+1} - r_{i-1})/2$, and $d\phi = 0.035$ radian,

which is the grid spacing in the ϕ direction. We focus on the results when the rope is within 1 au, referring to the CME Earth arrival. This figure shows that the rope holds a nearly radial propagation in the interplanetary space though it is deflected to the west slightly at first. Due to the simulation grid spacing in the ϕ direction, the axis in reality may not be solely located at the grid border. Thus, there exists an uncertainty of $\leq 2^\circ$ in locating the corresponding longitude, causing the variation of the green diamonds. Figure 4(b) gives the profiles of the traveling speeds of the rope front, axis and mass center in the radial direction, accompanied with the radial flow speed of the solar wind medium $10 R_s$ ahead of the rope. We can see that the flux rope is impulsively accelerated at first beneath $20 R_s$. After that, the red

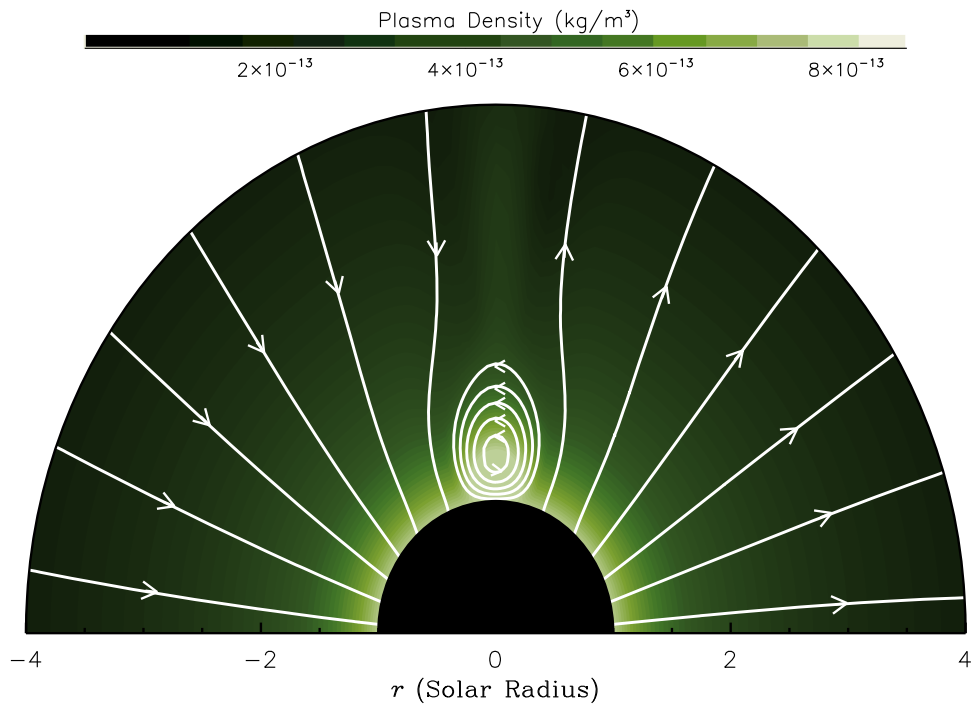


Figure 2. Magnetic structure of the flux rope system in a frame corotating with the Sun. Open solid white lines depict the magnetic field lines of the background and the arrows indicate the related directions. The flux rope is shown by the closed lines. The plasma density is shown in false color.

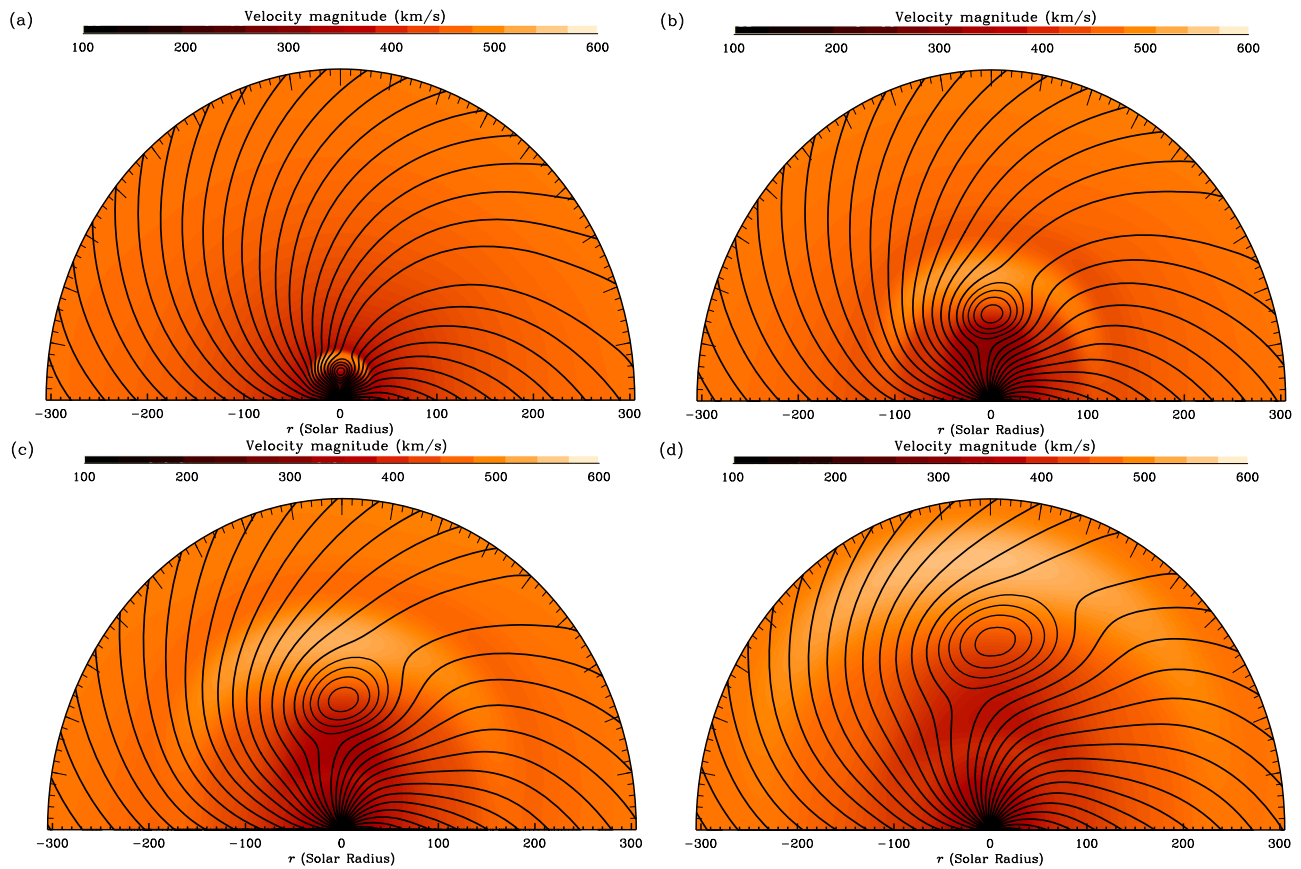


Figure 3. Eruption of the flux rope CME in the laboratory frame. The black open and closed lines indicate the magnetic field lines of the solar wind background and the flux rope, respectively. The velocity magnitude is shown in false color.

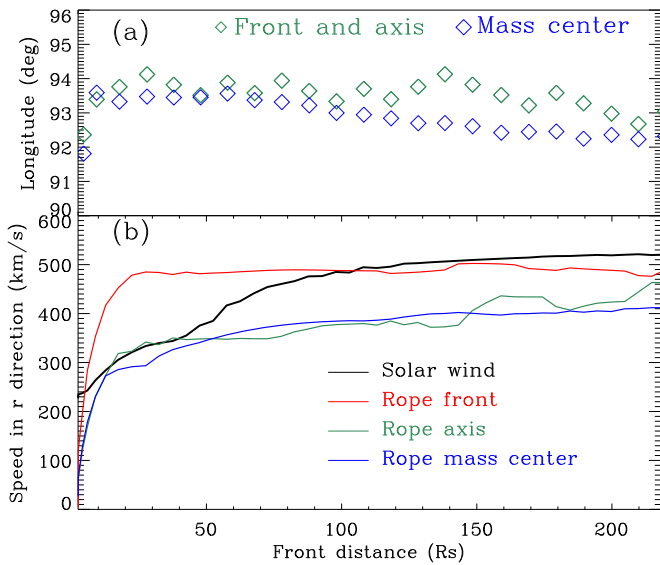


Figure 4. (a) The variations of the longitudes of the flux rope front (red), axis (green), and mass center (blue) along the front radial distance in the laboratory frame. The data points are plotted every 4 hr. (b) Profiles of the traveling speed of the flux rope front (red), axis (green), and mass center (blue), as well as the solar wind flow speed $10 R_s$ ahead of the rope (black) in the radial direction.

profile shows that the front of the rope is propagating at an approximate constant speed of about 500 km s^{-1} , which is very close to the solar wind speed beyond $100 R_s$, and the green and blue profiles show the continuous but smooth acceleration of the rope axis and mass center. The difference between the front speed and the axis (mass center) speed indicates the expansion of the rope in the radial direction.

3.3. Deflection of the Flux Rope with Different Traveling Speeds

The eruption driven by the catastrophe without extra acceleration methods (e.g., magnetic reconnection) will make the radial speed of the flux rope close to that of the solar wind medium in a short time. The small speed difference may lead to the rope radial propagation, as suggested by the DIPS model too. However, in reality, a flux rope can travel with a speed significantly different from that of the solar wind for a long time, like the “Bastille Day” event (e.g., Andrews 2001; Smith et al. 2001) or the “Halloween” event (e.g., Wang et al. 2005). Therefore, to simulate the flux rope that can hold a significant speed difference, we adjust the flux rope speed after the rope eruption at each calculation step as follows: (1) setting the maximum flow speed inside the rope in the radial direction (v_m) to be a constant v_{m0} ; (2) multiplying the radial flow speed at other grids in the rope by a common ratio of v_{m0}/v_m . Based on this adjustment, the flux rope will propagate at a nearly constant speed. Note that here we apply an “artificial viscosity” method to ψ during the simulation to maintain the stable calculation. We studied the cases with $v_{m0} = 300, 500, 800, 1000,$ and 1500 km s^{-1} , respectively. Figures 5(a)–(c) and Figures 5(e)–(g) show the propagation of the flux rope in the laboratory frame under the conditions of $v_{m0} = 300$ and 1500 km s^{-1} , respectively. It is found that the flux rope that travels slower or faster than the solar wind medium will be deflected to the west or east in the interplanetary space.

Figures 5(c) and (g) plot the background magnetic field lines with denser contour curves, and each curve is defined by a specific value of ψ , while ψ is divided into different values with uniform spacing. A region with denser contour curves indicates the pile up of the magnetic field lines in that region, and thus the stronger field strength (recalling Equation (6)). We can see that the magnetic field is stronger behind and to the right of, and ahead of and to the left of the rope, respectively, pushing the rope to the west and east. Figures 5(d) and (h) give the same schematic pictures of slow and fast CME propagation in the interplanetary medium in Wang et al. (2004), in which the “push” or “block” effect on the CME is consistent with our simulation. Besides, we find that the flux rope is flattened during the propagation, which seems to be caused by the squeezing of the magnetic field on the rope’s right side in Figure 5(c) and on both sides of the rope in Figure 5(g), respectively. Several studies have shown that the cross section of a flux rope could deviate from a circular shape (e.g., Manchester et al. 2004b; Riley & Crooker 2004; Chané et al. 2006; Savani et al. 2011; Isavnin 2016), or even form a convex-outward “pancake” shape.

Figure 6 plots the variations of the longitudes of the rope front, axis, and mass center versus the front distance with different v_{m0} , and the longitudinal variations in Figure 4(a) are also shown for comparison. There are several points to understand in the figure. First, the profiles of the case of $v_{m0} = 500 \text{ km s}^{-1}$ (brown) shows the radial propagation of the rope, which is similar to that of the case without adjusting the rope radial speed (black). Second, the deflection angle could reach 10° or even larger. Third, the larger v_{m0} is, indicating the faster propagation of the rope, the greater the deflection angle will be. Fourth, the profiles of the mass center are similar to those of the axis, but the deflection angles are found to be slightly larger. Fifth, the initial eastward deflection of the rope with $v_{m0} = 300 \text{ km s}^{-1}$ may be due to the smaller solar wind speed near the Sun.

4. Comparison with the DIPS Model

The above simulation supports the picture given by the DIPS model. In order to test the reliability of the DIPS model used in space weather forecasting, we compare our simulated results with the model predictions. The DIPS model requires the CME radial speed (v_r) and the solar wind speed (v_{sw}). The corresponding expression is

$$\Delta\phi(t) = \frac{v_{sw} - v_r}{v_{sw}} \Omega t, \quad (16)$$

where $\Delta\phi(t)$ is the time-dependent deflection angle. For the usual usage of the DIPS model, v_r is derived by coronagraph images and v_{sw} can be obtained by some empirical or MHD methods (e.g., Odstrcil & Pizzo 1999; Shen et al. 2007, 2018; Nakamizo et al. 2009). We then use the traveling speeds of the front, axis, and mass center of the flux rope to represent v_r , respectively, and use the radial flow speed $10 R_s$ ahead of the rope to represent v_{sw} . The background solar wind is selected such that it is not far away from the rope structure and also not close to the rope to be disturbed significantly, and the reliability of this selection is discussed in Section 5. The deflection angle is derived by the integration of Equation (16). Figure 7 plots the temporal variations of the longitudes predicted by the DIPS model with solid lines, and those

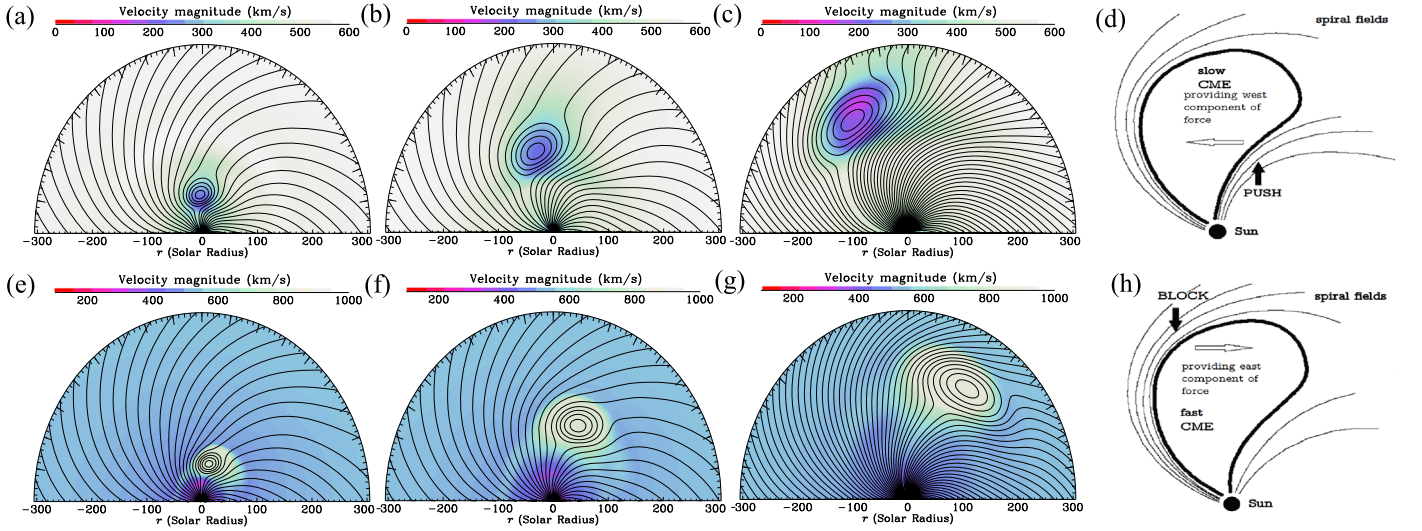


Figure 5. Westward and eastward deflection of the flux rope in the laboratory frame with $v_{m0} = 300$ and $v_{m0} = 1500 \text{ km s}^{-1}$ in panels (a)–(c) and (d)–(f), respectively. Panels (c) and (g) plot the background magnetic field lines with denser contour curves. The closed lines plot the flux rope structure, and the open lines show the background magnetic field. The false color shows the flow velocity magnitude. Panels (d) and (h) give the same schematic pictures of slow and fast CME propagation in the interplanetary medium in Wang et al. (2004; reprints and with permissions).

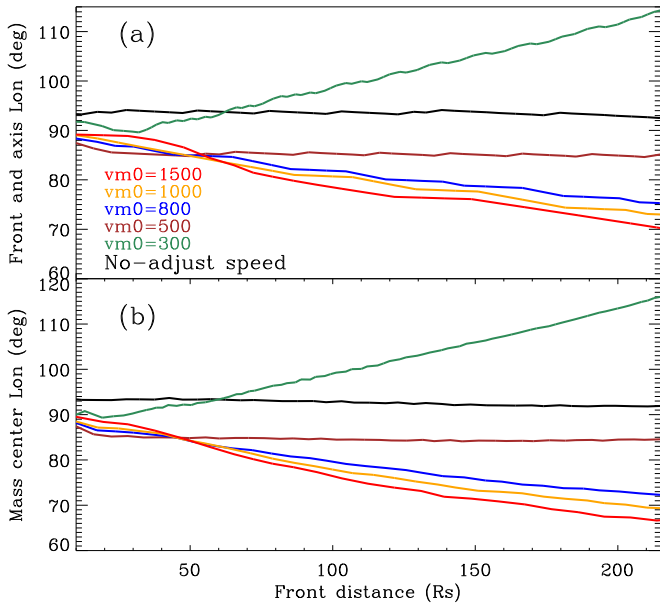


Figure 6. Variations of the longitudes of the rope front, axis, and mass center along the rope front distance from 10 to 215 R_s in the laboratory frame with $v_{m0} = 300 \text{ km s}^{-1}$ (green), 500 km s^{-1} (brown), 800 km s^{-1} (blue), 1000 km s^{-1} (orange), and 1500 km s^{-1} (red), accompanied with the case without adjusting rope speed (black). The arrows indicate the west/east directions.

in the simulations with diamonds. In Figure 7(a), illustrating the results without adjusting the rope speed, the prediction with rope front speed (red) inputted shows a nearly radial propagation of the rope after 20 hr, which is consistent with the simulation, though the DIPS model gives an eastward deflection of about 10° of the rope front at first. As for the axis (green) and mass center (blue), the related smaller rope speeds, which correspond to the rope radial expansion (as shown in Figure 4(b)), lead to the improper predictions of the significantly westward deflection. The DIPS model predictions with $v_{m0} = 500 \text{ km s}^{-1}$ in Figure 7(b) are

similar to those in Figure 7(a). In Figures 7(c)–(e) with $v_{m0} = 800$, 1000 and 1500 km s^{-1} , respectively, the predicted profiles behave in a similar fashion to each other and to the simulated data points. The results with the speeds of the axis and mass center inputted are closest to the related simulated data points, but those with the front speeds inputted result in larger deflection angles of few degrees. In Figure 7(f), the predictions are consistent with the simulated results, and among the profiles the red one is closest to the corresponding diamonds. Moreover, as shown in Figures 5(c) and (d), the “push” effect is behind the slow rope, and thus we estimate the deflection angle of this slowest rope by inputting the traveling speed of the rope tail and the radial flow speed of the solar wind $10 R_s$ behind the tail into the DIPS model (orange). Here the rope tail is the lowermost field line of the rope along the Sun-axis line, and the value of $10 R_s$ causes the related data points to start at 20 hr. The orange profile is found to be almost the same as the red one. Overall, the prediction of the DIPS model can have good consistency with the simulations. Furthermore, based on Figure 7, we think that the input of the rope front speed, which is easy to be obtained through observations, into the DIPS model can lead to reliable CME trajectory predictions, except for those traveling at a speed similar to the ambient solar wind.

5. Conclusions and Discussions

In this work, we numerically study the deflection of CMEs in the heliospheric equatorial plane. Our simulations demonstrate the deflection of a CME with flux rope structure in the interplanetary space, and confirm that the deflection is related to the speed difference between the rope and the solar wind medium. We find that a CME, which travels slower or faster than the solar wind medium, will be deflected to the west or east; the greater the difference between the CME speed and the solar wind speed is, the larger the deflection angle will be. This phenomenon may be interpreted as follows: (1) a slow CME can make the interplanetary magnetic field corotating with the Sun pile up behind and to the east of itself, while a fast CME leads to the pileup ahead and to the west of itself; (2) the

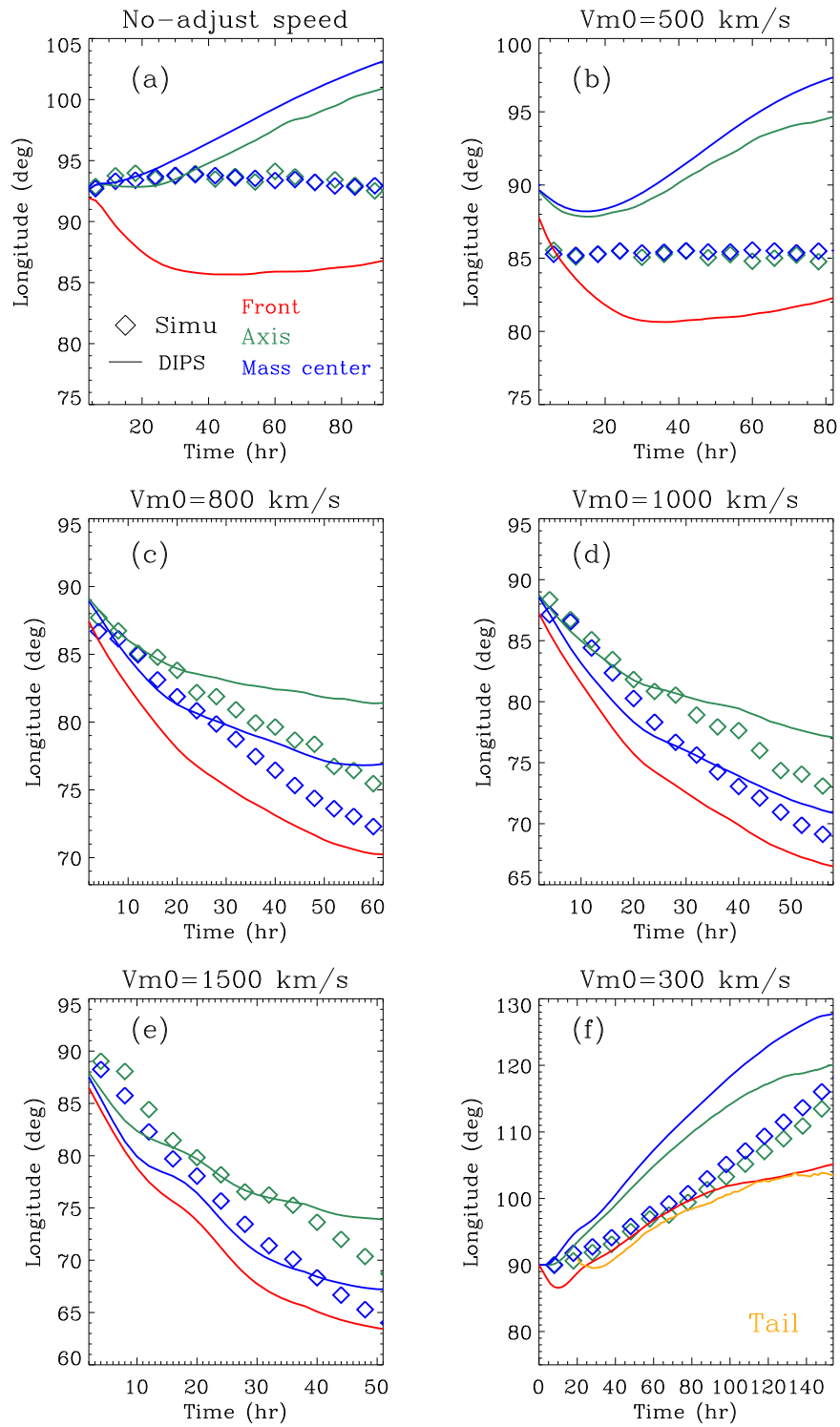


Figure 7. Variations of the longitudes of the flux rope in the simulation and estimated by the DIPS model. The solid lines show the results of the DIPS model and the diamonds show the simulated results. The red, green, blue, and orange colors indicate the results of the rope front, axis, mass center, and tail, respectively. The simulated data points in Figures (a)–(e) and (f) are plotted every 4 and 10 hr, respectively.

magnetic field in the piled-up region will become stronger; (3) the piled magnetic field then drives the corresponding deflection; and (4) the speed difference is related to the piled magnetic field strength. We compare the rope deflection angles in our simulations with those predicted by the DIPS model, and find that the predictions can have good consistency with the

simulated results, suggesting the effectiveness of the DIPS model used in space weather forecasting. Our simulations, though very ideal compared to a 3D one, can provide a stepstone toward studying CME deflection theoretically.

In the simulations, the CME is propagating at a nearly constant speed by the speed adjustment. However, in reality, a

CME will be decelerated or accelerated in the interplanetary space due to the drag force provided by the solar wind (e.g., Borgazzi et al. 2009; Subramanian et al. 2012), making the speed of a CME approach the solar wind speed. Thus, the real deflection angle may be smaller than that provided by our simulations. In the future, we will try some methods closer to reality to obtain a more appropriate propagation of a CME. Furthermore, we take a uniform γ for the whole domain, and this γ is quite high in the heliosphere (compared to $\gamma = 5/3$ in the model of Usmanov et al. 2000), which makes the solar wind speed always increase over 0.1 au (see Figure 4). However, it is still worthwhile since we are focusing on the relationship between the deflection and the speed differences. The simulations with a more realistic solar wind model including acceleration and heating processes will be developed in the future.

Before ending this paper, we would like to discuss the reliability of the DIPS model by inputting different solar wind backgrounds. Figure 8 shows the same cases as in Figure 7. The dashed-dotted, dotted, solid, and dashed profiles show the deflection angles by inputting the same rope front speed and the solar wind speed in front of the ropes of 2, 5, 10, and 20 R_s into the DIPS model, respectively. Different inputs of the solar wind speeds lead to more or less different predictions. In Figures 8(a) and (b), though the dashed profiles are closest to the simulated data point, there is no significant difference among the four types of profiles, except the eastward deflection at first. In Figures 8(c) to (f), considering the difference between the predicted and simulated data points and the trends of the profiles, the usage of the speed of the solar wind 10 R_s ahead of the rope is the best compromise in our simulation. Overall, when using the DIPS model, one should be cautious about selecting the appropriate background solar wind.

This work was supported the grants from NSFC (41774178, 41574165, 41274173, and 41804161), and the fundamental research funds for the central universities. We also acknowledge funds from Key Laboratory of Space Weather, National Center for Space Weather, China Meteorological Administration.

Appendix

Here we describe the multistep implicit scheme based on the 2.5D problems in the heliospheric equatorial plane, and one can also refer to Hu (1989) for the original introduction. The set of MHD Equations (7)–(14) in Section 2 can be written as

$$\frac{\partial U}{\partial t} + W \left(U, \frac{\partial U}{\partial r}, \frac{\partial U}{\partial \phi}, \frac{\partial^2 U}{\partial r^2}, \frac{\partial^2 U}{\partial \phi^2} \right) = 0, \quad (17)$$

where $U = (\rho, v_r, v_\theta, v_\phi, \psi, B_\theta, T)$. The expression of the vector W can be derived in a straightforward way and is omitted for conciseness. This scheme is implemented in three steps. In the following, a superscript n as well as subscripts i and j denote the points (t^n, r_i, ϕ_j) in the time-space mesh. Starting the first step of the split-implicit treatment in the r -direction,

Equation (17) reads

$$\frac{\bar{U}_{ij}^{n+1} - U_{ij}^n}{\Delta t} + \bar{W}_{ij}^{n+1} = 0, \quad (18)$$

where a bar over the top indicates intermediate quantities, and

$$\begin{aligned} \bar{W}_{ij}^{n+1} = & W^n + \left(\frac{\partial W}{\partial U} \right)^n [\bar{U}^{n+1} - U^n] \\ & + \left(\frac{\partial W}{\partial(\partial U/\partial r)} \right)^n \left[\left(\frac{\partial \bar{U}}{\partial r} \right)^{n+1} - \left(\frac{\partial U}{\partial r} \right)^n \right] \\ & + \left(\frac{\partial W}{\partial(\partial^2 U/\partial r^2)} \right)^n \left[\left(\frac{\partial^2 \bar{U}}{\partial r^2} \right)^{n+1} - \left(\frac{\partial^2 U}{\partial r^2} \right)^n \right]. \end{aligned} \quad (19)$$

Here the subscripts of i and j are expressly implied for all quantities on the right side of Equation (19). By using a central difference approximation for all the derivatives with respect to r at t^{n+1} , we reach the difference expression of Equation (18) as

$$A_{ij} \bar{U}_{ij}^{n+1} + B_{ij} \bar{U}_{i+1,j}^{n+1} + C_{ij} \bar{U}_{i-1,j}^{n+1} = E_{ij}, \quad (20)$$

where A_{ij} , B_{ij} , C_{ij} , and E_{ij} are written as

$$\begin{aligned} A_{ij} = & \frac{I}{\Delta t} + \left(\frac{\partial W}{\partial U} \right)_{ij}^n \\ & - \frac{2}{\Delta r_{i+1/2} \Delta r_{i-1/2}} \left(\frac{\partial W}{\partial(\partial^2 U/\partial r^2)} \right)_{ij}^n, \end{aligned} \quad (21)$$

$$\begin{aligned} B_{ij} = & \frac{1}{\Delta r_i \Delta r_{i+1/2}} \left(\frac{\partial W}{\partial(\partial^2 U/\partial r^2)} \right)_{ij}^n \\ & + \frac{1}{2\Delta r_i} \left(\frac{\partial W}{\partial(\partial U/\partial r)} \right)_{ij}^n \end{aligned} \quad (22)$$

$$\begin{aligned} C_{ij} = & \frac{1}{\Delta r_i \Delta r_{i-1/2}} \left(\frac{\partial W}{\partial(\partial^2 U/\partial r^2)} \right)_{ij}^n \\ & - \frac{1}{2\Delta r_i} \left(\frac{\partial W}{\partial(\partial U/\partial r)} \right)_{ij}^n \end{aligned} \quad (23)$$

$$\begin{aligned} E_{ij} = & -W_{ij}^n + \left[\frac{I}{\Delta t} + \left(\frac{\partial W}{\partial U} \right)_{ij}^n \right] U_{ij}^n \\ & + \left(\frac{\partial W}{\partial(\partial U/\partial r)} \right)_{ij}^n \left(\frac{\partial U}{\partial r} \right)_{ij}^n \\ & + \left(\frac{\partial W}{\partial(\partial^2 U/\partial r^2)} \right)_{ij}^n \left(\frac{\partial^2 U}{\partial r^2} \right)_{ij}^n. \end{aligned} \quad (24)$$

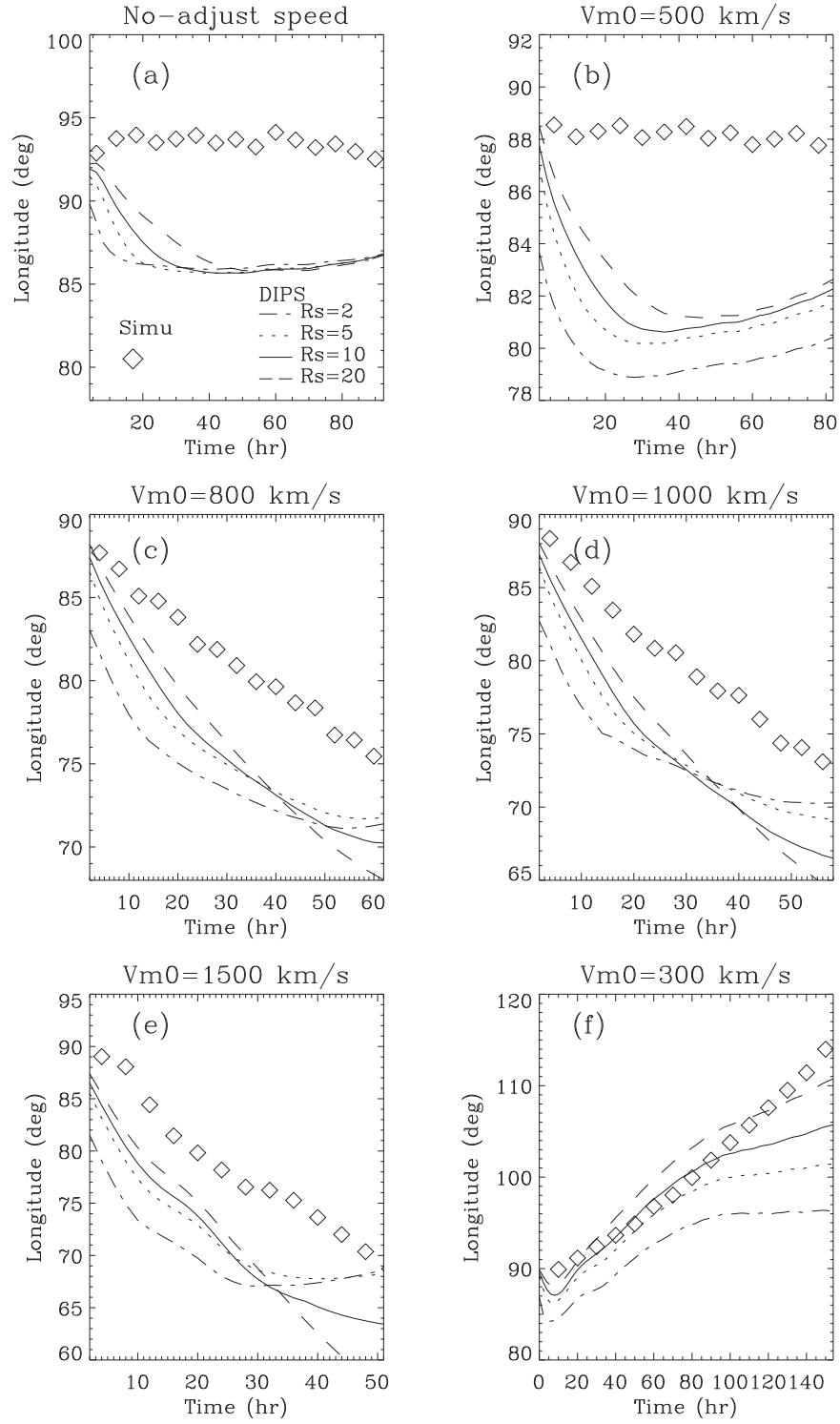


Figure 8. Profiles of the DIPS model predictions by inputting the flux rope front speeds, the same as those in Figure 7, and the solar wind speed in front of the rope at 2 (dashed-dotted), 5 (dotted), 10 (solid), and 20 (dashed) R_s . The diamonds are the simulated data points.

I is the unit matrix, and

$$\begin{aligned} \Delta r_i &= \frac{1}{2}(r_{i+1} - r_{i-1}), \quad \Delta r_{i+1/2} = (r_{i+1} - r_i), \\ \Delta r_{i-1/2} &= (r_i - r_{i-1}). \end{aligned} \quad (25)$$

For the second step, by using the split-implicit treatment in the ϕ -direction, we have

$$\frac{\bar{U}_{ij}^{n+2} - \bar{U}_{ij}^{n+1}}{\Delta t} + \bar{W}_{ij}^{n+2} = 0, \quad (26)$$

where

$$\begin{aligned} \bar{W}_{ij}^{n+2} &= \bar{W}^{n+1} + \left(\frac{\partial \bar{W}}{\partial \bar{U}} \right)^{n+1} [\bar{U}^{n+2} - \bar{U}^{n+1}] \\ &+ \left(\frac{\partial \bar{W}}{\partial(\partial \bar{U} / \partial \phi)} \right)^{n+1} \left[\left(\frac{\partial \bar{U}}{\partial \phi} \right)^{n+2} - \left(\frac{\partial \bar{U}}{\partial \phi} \right)^{n+1} \right] \\ &+ \left(\frac{\partial \bar{W}}{\partial(\partial^2 \bar{U} / \partial \phi^2)} \right)^{n+1} \left[\left(\frac{\partial^2 \bar{U}}{\partial \phi^2} \right)^{n+2} - \left(\frac{\partial^2 \bar{U}}{\partial \phi^2} \right)^{n+1} \right]. \end{aligned} \quad (27)$$

Similarly, the subscripts of i and j are expressly implied on the right side, and $\Delta \phi_j$ and $\Delta \phi_{j\pm 1/2}$ share similar notations as those shown in Equation (25). The difference expression of Equation (26) is

$$A'_{ij} \bar{U}_{ij}^{n+2} + B'_{ij} \bar{U}_{i,j+1}^{n+2} + C'_{ij} \bar{U}_{i,j-1}^{n+2} = E'_{ij}, \quad (28)$$

in which A'_{ij} , B'_{ij} , C'_{ij} , and E'_{ij} are given as

$$\begin{aligned} A'_{ij} &= \frac{I}{\Delta t} + \left(\frac{\partial \bar{W}}{\partial \bar{U}} \right)_{ij}^{n+1} \\ &- \frac{2}{\Delta \phi_{j+1/2} \Delta \phi_{j-1/2}} \left(\frac{\partial \bar{W}}{\partial(\partial^2 \bar{U} / \partial \phi^2)} \right)_{ij}^{n+1}, \end{aligned} \quad (29)$$

$$\begin{aligned} B'_{ij} &= \frac{1}{\Delta \phi_j \Delta \phi_{j+1/2}} \left(\frac{\partial \bar{W}}{\partial(\partial^2 \bar{U} / \partial \phi^2)} \right)_{ij}^{n+1} \\ &+ \frac{1}{2 \Delta \phi_j} \left(\frac{\partial \bar{W}}{\partial(\partial \bar{U} / \partial \phi)} \right)_{ij}^{n+1} \end{aligned} \quad (30)$$

$$\begin{aligned} C'_{ij} &= \frac{1}{\Delta \phi_j \Delta \phi_{j-1/2}} \left(\frac{\partial \bar{W}}{\partial(\partial^2 \bar{U} / \partial \phi^2)} \right)_{ij}^{n+1} \\ &- \frac{1}{2 \Delta \phi_j} \left(\frac{\partial \bar{W}}{\partial(\partial \bar{U} / \partial \phi)} \right)_{ij}^{n+1} \end{aligned} \quad (31)$$

$$\begin{aligned} E'_{ij} &= -\bar{W}_{ij}^n + \left[\frac{I}{\Delta t} + \left(\frac{\partial \bar{W}}{\partial \bar{U}} \right)_{ij}^{n+1} \right] \bar{U}_{ij}^{n+1} \\ &+ \left(\frac{\partial \bar{W}}{\partial(\partial \bar{U} / \partial \phi)} \right)_{ij}^{n+1} \left(\frac{\partial \bar{U}}{\partial \phi} \right)_{ij}^{n+1} \\ &+ \left(\frac{\partial \bar{W}}{\partial(\partial^2 \bar{U} / \partial \phi^2)} \right)_{ij}^{n+1} \left(\frac{\partial^2 \bar{U}}{\partial \phi^2} \right)_{ij}^{n+1}. \end{aligned} \quad (32)$$

Finally, for the third step, an arithmetic average between U^n and \bar{U}^{n+2} is taken to get U^{n+1} for the new time step, i.e.,

$$U^{n+1} = \frac{U^n + \bar{U}^{n+2}}{2}. \quad (33)$$

ORCID iDs

Bin Zhuang  <https://orcid.org/0000-0002-5996-0693>
 Yuming Wang  <https://orcid.org/0000-0002-8887-3919>
 Rui Liu  <https://orcid.org/0000-0003-4618-4979>
 Tingyu Gou  <https://orcid.org/0000-0003-0510-3175>
 Quanhao Zhang  <https://orcid.org/0000-0003-0565-3206>

References

- Andrews, M. D. 2001, *SoPh*, **204**, 179
- Borgazzi, A., Lara, A., Echer, E., & Alves, M. V. 2009, *A&A*, **498**, 885
- Capannolo, L., Opher, M., Kay, C., & Landi, E. 2017, *ApJ*, **839**, 37
- Chané, E., van der Holst, B., Jacobs, C., Poedts, S., & Kimpe, D. 2006, *A&A*, **447**, 727
- Chen, J., Howard, R. A., Brueckner, G. E., et al. 1997, *ApJL*, **490**, L191
- Chen, J., & Krall, J. 2003, *JGRA*, **108**, 1410
- Chen, Y., Hu, Y. Q., & Sun, S. J. 2007, *ApJ*, **665**, 1421
- Cid, C., Cremades, H., Aran, A., et al. 2012, *JGRA*, **117**, A11102
- Cremades, H., & Bothmer, V. 2004, *A&A*, **422**, 307
- Dasso, S., Mandrini, C. H., Démoulin, P., & Luoni, M. L. 2006, *A&A*, **455**, 349
- DeForest, C. E., Howard, T. A., & McComas, D. J. 2013, *ApJ*, **769**, 43
- Dere, K. P., Brueckner, G. E., Howard, R. A., Michels, D. J., & Delaboudiniere, J. P. 1999, *ApJ*, **516**, 465
- Forbes, T. G. 2000, *JGR*, **105**, 23153
- Gosling, J. T. 2012, *SSRv*, **172**, 187
- Gosling, J. T., Bame, S. J., McComas, D. J., & Phillips, J. L. 1990, *GeoRL*, **17**, 901
- Gui, B., Shen, C., Wang, Y., et al. 2011, *SoPh*, **271**, 111
- Howard, R. A., Michels, D. J., Sheeley, N. R., Jr., & Koomen, M. J. 1982, *ApJL*, **263**, L101
- Hu, Y. 1989, *JCoPh*, **84**, 441
- Hu, Y. Q. 2001, *SoPh*, **200**, 115
- Hu, Y. Q., Li, G. Q., & Xing, X. Y. 2003, *JGRA*, **108**, 1072
- Isavnin, A. 2016, *ApJ*, **833**, 267
- Kay, C., Opher, M., & Evans, R. M. 2013, *ApJ*, **775**, 5
- Lugaz, N. 2010, *SoPh*, **267**, 411
- Lugaz, N., Downs, C., Shibata, K., et al. 2011, *ApJ*, **738**, 127
- Lugaz, N., Farrugia, C. J., Davies, J. A., et al. 2012, *ApJ*, **759**, 68
- Lugaz, N., Temmer, M., Wang, Y., & Farrugia, C. J. 2017, *SoPh*, **292**, 64
- Manchester, W. B., Gombosi, T. I., Roussev, I., et al. 2004a, *JGRA*, **109**, A01102
- Manchester, W. B., Gombosi, T. I., Roussev, I., et al. 2004b, *JGRA*, **109**, A02107
- Möstl, C., Rollett, T., Frahm, R. A., et al. 2015, *NatCo*, **6**, 7135
- Nakamizo, A., Tanaka, T., Kubo, Y., et al. 2009, *JGRA*, **114**, A07109
- Odstrcil, D., & Pizzo, V. J. 1999, *JGR*, **104**, 28225
- Riley, P., & Crooker, N. U. 2004, *ApJ*, **600**, 1035
- Riley, P., Linker, J. A., Mikić, Z., et al. 2003, *JGRA*, **108**, 1272
- Ruffenach, A., Lavraud, B., Farrugia, C. J., et al. 2015, *JGRA*, **120**, 43
- Ruffenach, A., Lavraud, B., Owens, M. J., et al. 2012, *JGRA*, **117**, A09101
- Savani, N. P., Owens, M. J., Rouillard, A. P., et al. 2011, *ApJ*, **731**, 109
- Shen, C., Wang, Y., Gui, B., Ye, P., & Wang, S. 2011, *SoPh*, **269**, 389
- Shen, C., Wang, Y., Wang, S., et al. 2012, *NatPh*, **8**, 923
- Shen, F., Feng, X., Wu, S. T., & Xiang, C. 2007, *JGRA*, **112**, A06109
- Shen, F., Shen, C., Wang, Y., Feng, X., & Xiang, C. 2013, *GeoRL*, **40**, 1457
- Shen, F., Shen, C., Zhang, J., et al. 2014, *JGRA*, **119**, 7128
- Shen, F., Wang, Y., Shen, C., & Feng, X. 2017, *SoPh*, **292**, 104
- Shen, F., Yang, Z., Zhang, J., Wei, W., & Feng, X. 2018, *ApJ*, **866**, 18
- Shiota, D., & Kataoka, R. 2016, *SpWea*, **14**, 56
- Shiota, D., Kusano, K., Miyoshi, T., & Shibata, K. 2010, *ApJ*, **718**, 1305
- Smith, C. W., Ness, N. F., Burlaga, L. F., et al. 2001, *SoPh*, **204**, 227
- Srivastava, N., & Venkatakrishnan, P. 2004, *JGRA*, **109**, A10103
- Subramanian, P., Lara, A., & Borgazzi, A. 2012, *GeoRL*, **39**, L19107
- Sun, S. J., & Hu, Y. Q. 2005, *JGRA*, **110**, A05102
- Török, T., Downs, C., Linker, J. A., et al. 2018, *ApJ*, **856**, 75
- Usmanov, A. V., Goldstein, M. L., Besser, B. P., & Fritzer, J. M. 2000, *JGR*, **105**, 12675
- Vandas, M., Fischer, S., Dryer, M., Smith, Z., & Detman, T. 1996, *JGR*, **101**, 2505
- Vourlidas, A., Lynch, B. J., Howard, R. A., & Li, Y. 2013, *SoPh*, **284**, 179
- Wang, Y., Chen, C., Gui, B., et al. 2011, *JGRA*, **116**, A04104
- Wang, Y., Shen, C., Liu, R., et al. 2018, *JGRA*, **123**, 3238
- Wang, Y., Shen, C., Wang, S., & Ye, P. 2004, *SoPh*, **222**, 329
- Wang, Y., Wang, B., Shen, C., Shen, F., & Lugaz, N. 2014, *JGRA*, **119**, 5117
- Wang, Y., Xue, X., Shen, C., et al. 2006, *ApJ*, **646**, 625
- Wang, Y., Ye, P., Zhou, G., et al. 2005, *SoPh*, **226**, 337
- Wang, Y., Zhang, Q., Liu, J., et al. 2016, *JGRA*, **121**, 7423
- Wang, Y. M., Ye, P. Z., Wang, S., Zhou, G. P., & Wang, J. X. 2002, *JGRA*, **107**, 1340
- Webb, D. F., Cliver, E. W., Crooker, N. U., Cry, O. C. S., & Thompson, B. J. 2000, *JGR*, **105**, 7491

Wu, C.-C., Fry, C. D., Wu, S. T., Dryer, M., & Liou, K. 2007, [JGRA](#), **112**, [A09104](#)
Xiong, M., Zheng, H., Wu, S. T., Wang, Y., & Wang, S. 2007, [JGRA](#), **112**, [A11103](#)
Yermolaev, Y. I., & Yermolaev, M. Y. 2006, [AdSpR](#), **37**, [1175](#)
Zhang, J., Dere, K. P., Howard, R. A., & Bothmer, V. 2003, [ApJ](#), **582**, [520](#)

Zhang, Q., Wang, Y., Hu, Y., Liu, R., & Liu, J. 2017, [ApJ](#), **835**, [211](#)
Zhou, Y., & Feng, X. 2017, [JGRA](#), **122**, [1451](#)
Zhou, Y. F., & Feng, X. S. 2013, [JGRA](#), **118**, [6007](#)
Zhuang, B., Hu, Y., Wang, Y., et al. 2018, [JGRA](#), **123**, [2513](#)
Zhuang, B., Wang, Y., Shen, C., et al. 2017, [ApJ](#), **845**, [117](#)
Zuccarello, F. P., Bemporad, A., Jacobs, C., et al. 2012, [ApJ](#), **744**, [66](#)